Supplementary information

The C-type lectin receptor DCIR senses galactose-terminated N-glycans on LRP1 to regulate myeloid cell function

Benjamin B. A. Raymond,[1,6,10] Tamara Sneperger,[1,7,10] Stella Rousset,[1,10] Nelly Gilles,[1] Aurélie Bally,[1] Alexandre Stella,[1,2] Agnes L. Hipgrave Ederveen,[3] Samuel Tranier,[1] Julien Marcoux,[1,2] Giulia Trimaglio,[1,8] Thibaut Sanchez,[1,7] Vanessa Porkolab,[4,9] Corinne Vivès,[4] Michel Thépaut,[4] Frederic Lagarrigue,[1] Odile Burlet-Schiltz,[1,2] Manfred Wuhrer,[3] Franck Fieschi,[4,5] Pascal Demange,[1,11] Olivier Neyrolles[1,11] * and Yoann Rombouts[1,11,12] *

[1]Institut de Pharmacologie et de Biologie Structurale, IPBS, Université de Toulouse, CNRS, UPS, Toulouse, France

[2]Infrastructure Nationale de Protéomique, ProFI, UAR 2048, Toulouse, France

[3]Center for Proteomics and Metabolomics, Leiden University Medical Center, Leiden, The Netherlands

[4]Univ. Grenoble Alpes, CNRS, CEA, Institut de Biologie Structurale, Grenoble, France

[5]Institut Universitaire de France, Paris, France

[6]Present address: Biosciences Institute, Faculty of Medical Sciences, Newcastle University, Newcastle upon Tyne, United Kingdom

[7]Present address: Centre for Inflammation Research, University of Edinburgh, Edinburgh BioQuarter, Edinburgh, United Kingdom

[8]Present address: Institute for Clinical Chemistry and Laboratory Medicine, University Hospital and Faculty of Medicine, TU Dresden, 01307, Dresden, Germany and National Center for Tumor Diseases, Partner Site Dresden, 01307, Dresden, Germany

[9]Present address: Eurofins Cerep SA, 86600 Celle-Lévescault, France.

[10]These authors contributed equally

[11]These senior authors contributed equally

[12]Lead contact

*Correspondence: olivier.neyrolles@ipbs.fr (O.N), yoann.rombouts@ipbs.fr (Y.R.)

SUPPLEMENTARY TABLES

(in separate files)

Table S1: Proteins enriched by DCIR affinity pulldowns (related to figures 2C, 3B and S3B-C).

Table S2: Protein identifications from LRP1 immunoprecipitation (related to figure 2D).

Table S3: List and relative intensity of the N-glycans of human serum and mouse macrophage LRP1 α-chains as analyzed by CE-ESI-MS (related to figure 4B).

Table S4. Kinetic parameters resulting from SPR analysis using the kinetic 1:1 interaction model analysis for the interaction of hDCIR-ECD with different BSA-derived neoglycoconjugates (related to figure 4E).

Table S5: Crystallographic data collection and refinement statistics (related to figures 5A-B and 6A-C).

Table S6. Proteins enriched in WT macrophages compared to mDCIR1-KO macrophages following selective proteomic proximity labeling assay (related to figure S7B).

Table S7: List of antibodies used for flow cytometry experiments.

SUPPLEMENTARY FIGURES

Figure S1: Flow cytometry gating strategy for the analysis of immune cells extracted from tissues of WT and mDCIR1-KO mice (related to figure 1).

Figure S2: Flow cytometry analysis of mDCIR1$^+$ cells in the lung, spleen and thymus of mice (related to Figure 1).

Figure S3: LRP1 is a main glycoprotein ligand of mDCIR1 (related to figure 2)

Figure S4: Generation of LRP1-deficient macrophages (related to figures 2E and 3D).

Figure S5: Glycosylation analysis of mouse and human LRP1 (related to figure 4)

Figure S6: Structural analysis of hDCIR-ECD (related to figures 5 and 6).

Figure S7: Investigation of the spatial proximity between DCIR and LPR1, and the mechanism of DCIR activation (related to figure 7).

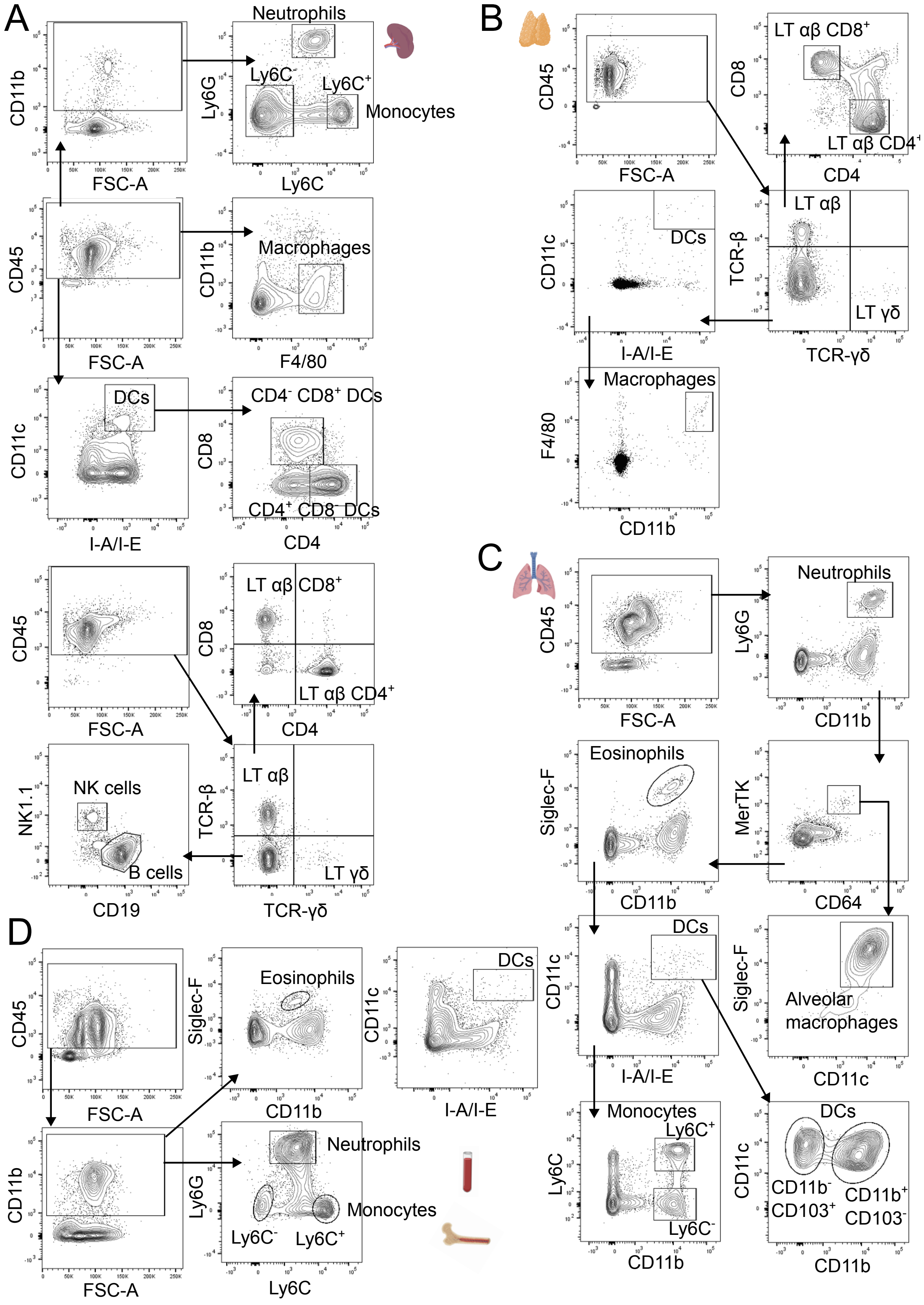
A
CD11b
FSC-A
Neutrophils
Ly6G
Ly6C-
Ly6C+
Monocytes
Ly6C
CD45
FSC-A
CD11b
Macrophages
F4/80
CD11c
DCs
I-A/I-E
CD8
CD4- CD8+ DCs
CD4+ CD8- DCs
CD4
CD45
FSC-A
CD8
LT αβ CD8+
LT αβ CD4+
CD4
NK1.1
NK cells
B cells
CD19
TCR-β
LT αβ
LT γδ
TCR-γδ
B
CD45
FSC-A
CD8
LT αβ CD8+
LT αβ CD4+
CD4
CD11c
DCs
I-A/I-E
TCR-β
LT αβ
LT γδ
TCR-γδ
F4/80
Macrophages
CD11b
C
CD45
FSC-A
Ly6G
Neutrophils
CD11b
Siglec-F
Eosinophils
CD11b
MerTK
CD64
CD11c
DCs
I-A/I-E
Siglec-F
Alveolar macrophages
CD11c
Ly6C
Monocytes
Ly6C+
Ly6C-
CD11b
CD11c
DCs
CD11b- CD103+
CD11b+ CD103-
CD11b
D
CD45
FSC-A
Siglec-F
Eosinophils
CD11b
CD11c
DCs
I-A/I-E
CD11b
FSC-A
Ly6G
Neutrophils
Monocytes
Ly6C-
Ly6C+
Ly6C

Figure S1: Flow cytometry gating strategy for the analysis of immune cells extracted from tissues of WT and mDCIR1-KO mice (related to figure 1).

(A) Gating strategy of myeloid and lymphoid cell subsets in the spleen of WT and mDCIR1-KO mice.

(B) Gating strategy of myeloid and lymphoid cell subsets in the thymus of WT and mDCIR1-KO mice.

(C) Gating strategy of myeloid in the lung of WT and mDCIR1-KO mice.

(D) Gating strategy of myeloid in the blood and bone marrow.

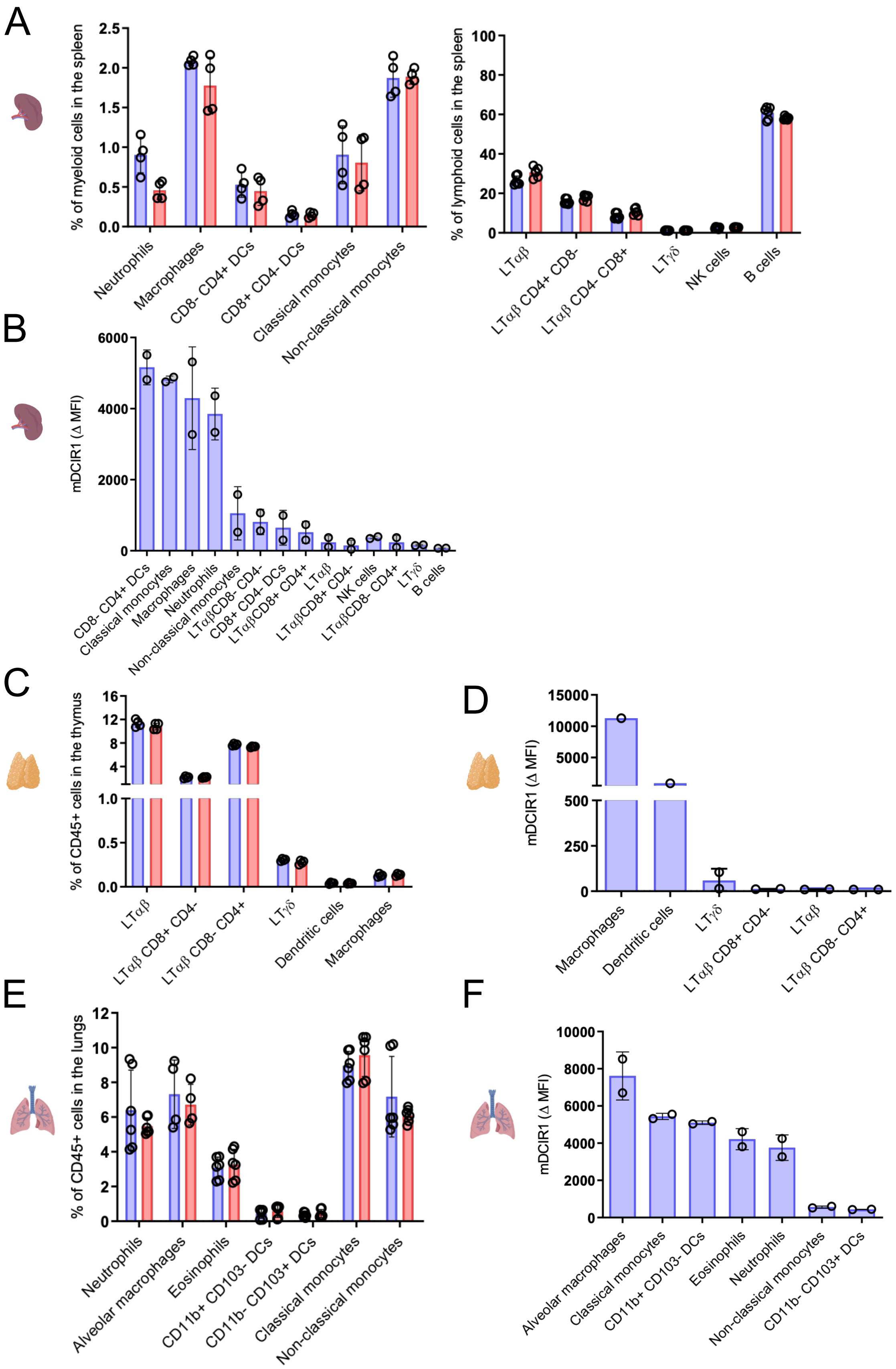
A
% of myeloid cells in the spleen
2.5
2.0
1.5
1.0
0.5
0.0
Neutrophils
Macrophages
CD8- CD4+ DCs
CD8+ CD4- DCs
Classical monocytes
Non-classical monocytes
% of lymphoid cells in the spleen
100
80
60
40
20
0
LTαβ
LTαβ CD4+ CD8-
LTαβ CD4- CD8+
LTγδ
NK cells
B cells
B
mDCIR1 (Δ MFI)
6000
4000
2000
0
CD8- CD4+ DCs
Classical monocytes
Macrophages
Neutrophils
Non-classical monocytes
LTαβCD8- CD4-
CD8+ CD4- DCs
LTαβCD8+ CD4+
LTαβ
LTαβCD8+ CD4-
NK cells
LTαβCD8- CD4+
LTγδ
B cells
C
% of CD45+ cells in the thymus
16
12
8
4
1.0
0.5
0.0
LTαβ
LTαβ CD8+ CD4-
LTαβ CD8- CD4+
LTγδ
Dendritic cells
Macrophages
D
mDCIR1 (Δ MFI)
15000
10000
5000
500
250
0
Macrophages
Dendritic cells
LTγδ
LTαβ CD8+ CD4-
LTαβ
LTαβ CD8- CD4+
E
% of CD45+ cells in the lungs
12
10
8
6
4
2
0
Neutrophils
Alveolar macrophages
Eosinophils
CD11b+ CD103- DCs
CD11b- CD103+ DCs
Classical monocytes
Non-classical monocytes
F
mDCIR1 (Δ MFI)
10000
8000
6000
4000
2000
0
Alveolar macrophages
Classical monocytes
CD11b+ CD103- DCs
Eosinophils
Neutrophils
Non-classical monocytes
CD11b- CD103+ DCs

Figure S2: Flow cytometry analysis of mDCIR1+ cells in the spleen, thymus and lung of mice (related to figure 1).

(A) Percentage of myeloid (left panel) and lymphoid cells (right panel) among immune cells ($CD45^+$) in the spleen of WT and mDCIR1-KO mice.

(B) Delta mean fluorescence intensity (ΔMFI) of mDCIR1 in myeloid and lymphoid cells in the spleen of WT mice. ΔMFI was calculated by subtracting the background fluorescence of mDCIR1 in mDCIR1-KO cell subsets from the mean fluorescence intensity (MFI) of mDCIR1 in the corresponding WT cell subsets.

(C) Percentage of myeloid and lymphoid cells among immune cells ($CD45^+$) in the thymus of WT and mDCIR1-KO mice.

(D) ΔMFI of mDCIR1 in myeloid and lymphoid cells in the thymus of WT mice.

(E) Percentage of myeloid cells among immune cells ($CD45^+$) in the lung of WT and mDCIR1-KO mice.

(F) ΔMFI of mDCIR1 in myeloid cells in the lung of WT mice.

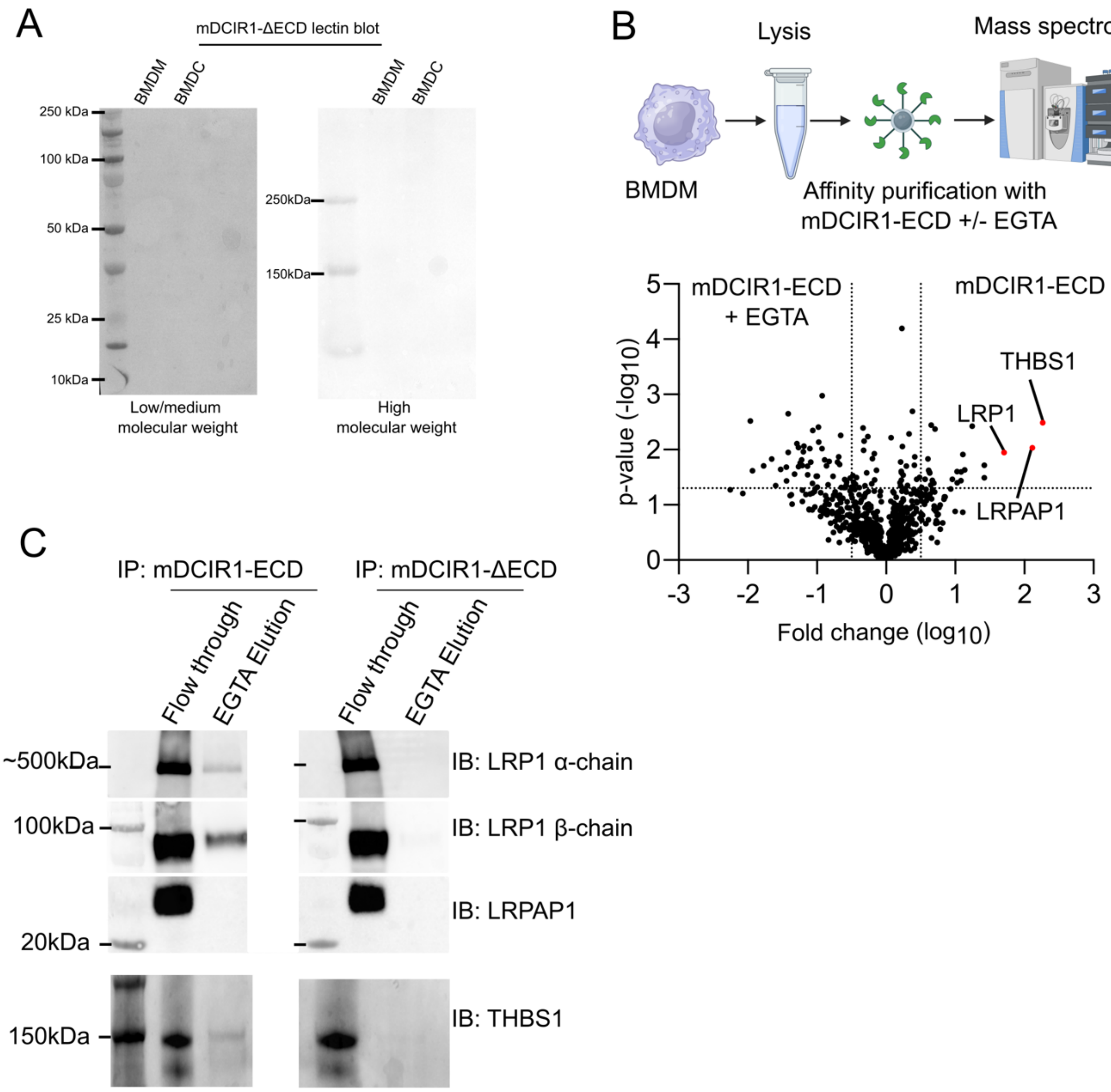

Figure S3: LRP1 is a main glycoprotein ligand of mDCIR1 (related to figure 2)

(A) Lectin blot examination of proteins extracted from BMDMs and BMDCs using biotinylated mDCIR1-ΔECD coupled to streptavidin-HRP.

(B) Schematic (top) of the enrichment of mDCIR1 ligand(s) from BMDMs by affinity purification using biotinylated mDCIR1-ECD (or in presence of divalent cation chelating agent EGTA as negative control) coupled to streptavidin beads and their subsequent identification by proteomics (Created with BioRender.com). Volcano Plot (bottom) from quantitative proteomics analysis of proteins differentially enriched (X-axis in $\log_{10}$) by affinity purification with mDCIR1-ECD versus mDCIR1-ECD with EGTA as a function of statistical significance (Y-axis in $-\log_{10}$). BMDMs are derived from 3 WT mice and were treated independently. Statistical analysis was performed using a paired Student's *t*-test. Dashed line marks the threshold limit ($\log_{10}$ fold change $\geq$ +/- 0.5 and $-\log_{10}$ *p*-value $\geq$ 1.301).

(C) Western blot analysis of LRP1, LRPAP1 and THBS1 after affinity purification of BMDM proteins using either mDCIR1-ECD or mDCIR1-ΔECD.

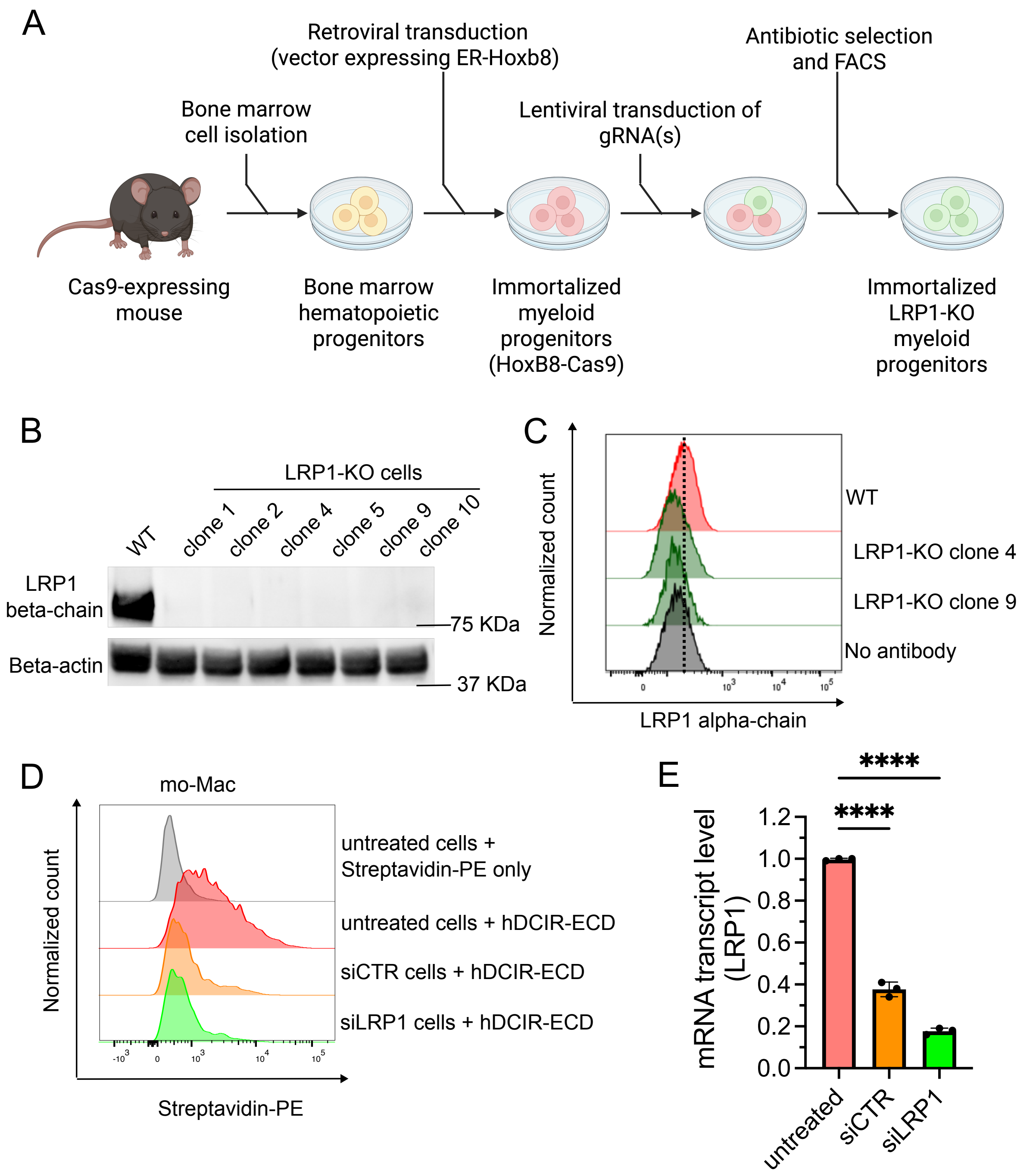

Figure S4: Generation of LRP1-deficient macrophages (related to figures 2E and 3D).

(A) Schematic of the protocol used to generate LRP1-deficient HoxB8 myeloid progenitors. Created with BioRender.com

(B) Western blot analysis of LRP1 β-chain in WT and six clones of LRP1-KO HoxB8-derived mouse macrophages.

(B) Flow cytometry analysis of LRP1 α-chain in WT and 2 clones of LRP1-KO HoxB8-derived mouse macrophages

(D) Flow cytometry histograms of the binding of biotinylated hDCIR-ECD coupled to Streptavidin-PE to human blood monocyte-derived macrophages (mo-Macs) non-transfected, or transfected with either a non-targeted siRNA pool (siCTR) or siRNA against LRP1 (siLRP1). (E) mRNA transcript level of LRP1 (in ddCT normalized on GAPDH transcript level in mo-Macs) non-transfected, or transfected with either a non-targeted siRNA pool (siCTR) or siRNA against LRP1 (siLRP1). Each data point corresponds to an individual replicate (N=3). Bars and error bars indicate the mean ± standard deviation. Statistical analysis was performed using a Dunnett's multiple comparisons test. **** indicates an adjusted *p*-value <0.0001.

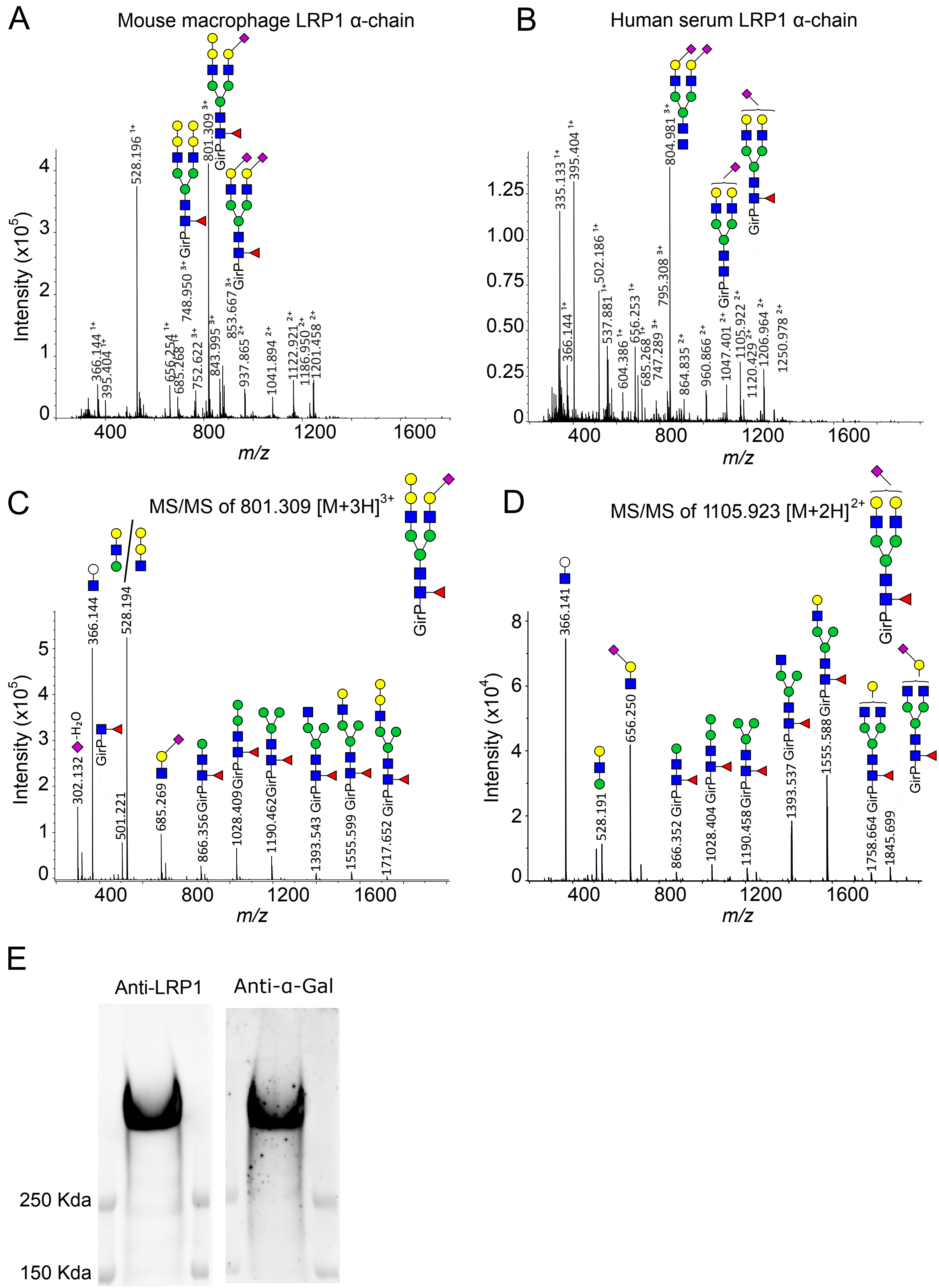
A
Mouse macrophage LRP1 α-chain
Intensity (x10^5)
0
1
2
3
4
400
800
1200
1600
m/z
366.144 1+
395.404 1+
528.196 1+
656.254 1+
685.268 1+
748.950 3+ GirP
752.622 3+
801.309 3+ GirP
843.995 3+
853.667 3+ GirP
937.865 2+
1041.894 2+
1122.921 2+
1186.950 2+
1201.458 2+
B
Human serum LRP1 α-chain
0
0.25
0.50
0.75
1.00
1.25
400
800
1200
1600
m/z
335.133 1+
366.144 1+
395.404 1+
502.186 1+
537.881 1+
604.386 1+
656.253 1+
685.268 1+
747.289 3+
795.308 3+
804.981 3+
864.835 2+
960.866 2+
1047.401 2+ GirP
1105.922 2+
1120.429 2+
1206.964 2+
1250.978 2+
GirP
C
MS/MS of 801.309 [M+3H]$^{3+}$
Intensity (x10^5)
0
1
2
3
4
5
400
800
1200
1600
m/z
302.132 -H$_2$O
366.144
501.221
528.194
GirP
685.269
866.356 GirP
1028.409 GirP
1190.462 GirP
1393.543 GirP
1555.599 GirP
1717.652 GirP
GirP
D
MS/MS of 1105.923 [M+2H]$^{2+}$
Intensity (x10^4)
0
2
4
6
8
400
800
1200
1600
m/z
366.141
528.191
656.250
866.352 GirP
1028.404 GirP
1190.458 GirP
1393.537 GirP
1555.588 GirP
1758.664 GirP
1845.699
GirP
GirP
E
Anti-LRP1
Anti-α-Gal
250 Kda
150 Kda

Figure S5: Glycosylation analysis of mouse and human LRP1 (related to figure 4)

(A) Summed mass spectrum (recorded between 40.1 and 43.6 min) of the CE-ESI-MS analysis of N-glycans derived from LRP1 α-chain of BMDMs. N-glycans were analyzed after sialic acid derivatization (ethyl esterification and amidation) and reducing end labelling with Girard's Reagent P (GirP). Blue square: N-acetylglucosamine, green circle: mannose, yellow circle: galactose, red triangle: fucose, right pointing purple diamond: α2,6-linked N-acetylneuraminic acid/sialic acid, left pointing purple diamond: α2,3-linked N-acetylneuraminic acid/sialic acid.

(B) Summed mass spectrum (recorded between 40.3 and 43.3 min) of the CE-ESI-MS analysis of N-glycans derived from human serum LRP1 α-chain. N-glycans were derivatized and labelled as in described in (A).

(C) CE-ESI-MS/MS fragmentation spectra of the precursor ions at 801.309^{3+} of the derivatized and labelled N-glycans derived from LRP1 of BMDMs.

(D) CE-ESI-MS/MS fragmentation spectra of the precursor ions at 1105.923^{2+} of the derivatized and labelled N-glycans from human serum LRP1.

(E) Western blot confirmation of the presence of α-Gal epitope on mouse LRP1 α-chain.

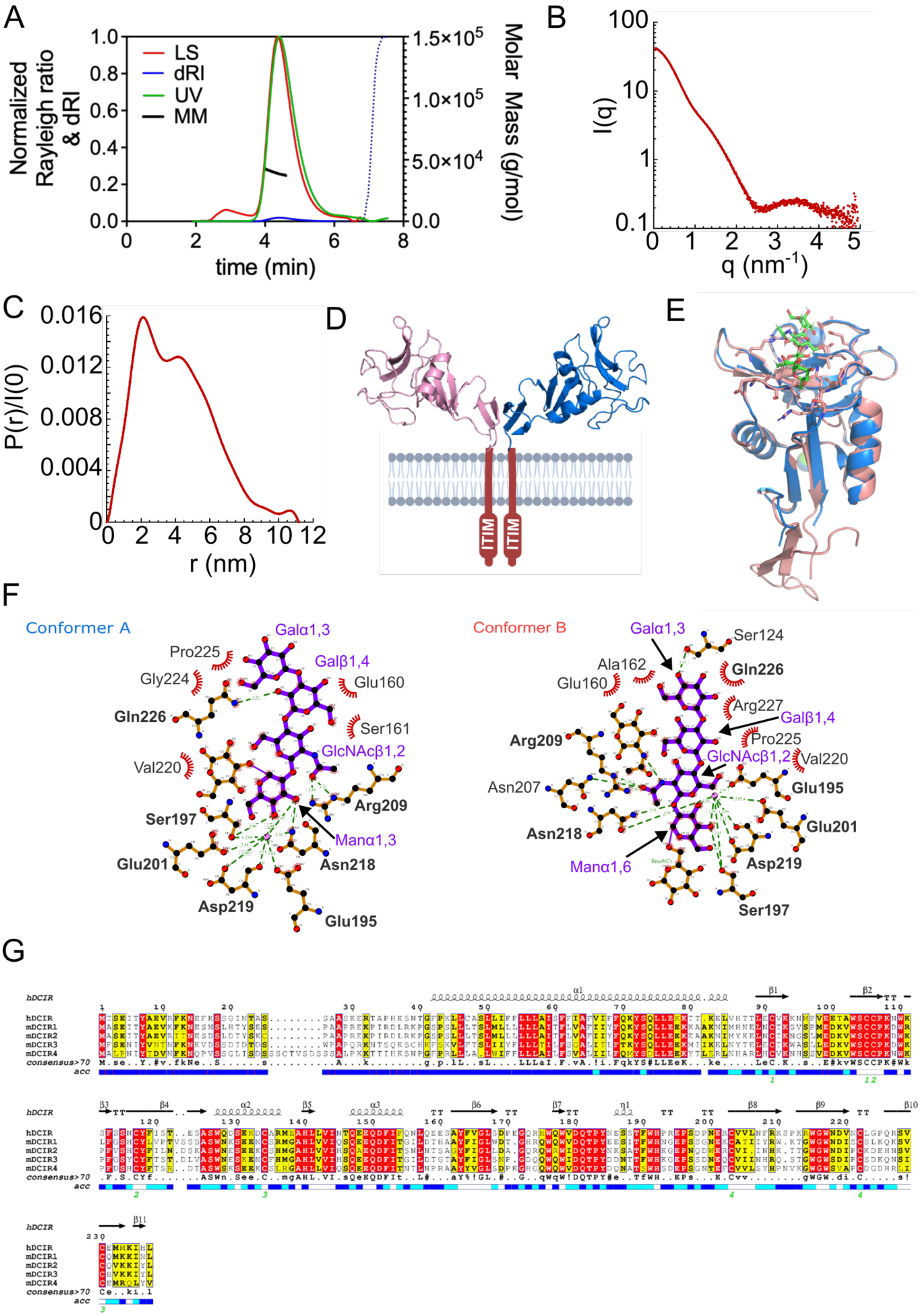

Figure S6: Structural analysis of hDCIR-ECD (related to figures 5 and 6).

(A) Confirmation of the dimeric conformation of hDCIR-ECD in solution by SEC-MALS/RI experiments. The eluted peak corresponds to a molecule with a mean molecular mass of 39.67 ± 1.57 kDa which is compatible with a dimeric species (theoretical molecular weight of the monomeric cleaved protein is 22.03 kDa). Hydrodynamic radius was measured at 3.25 +/- 0.09 nm and revealed compatible with a dimeric species. LS, dRI, UV and MM stand for light scattering, differential refractive index, ultraviolet-visible absorbance and molecular mass.

(B) and (C) are respectively the experimental scattered intensity I(q) curve and the distance distribution function P(r) of the hDCIR-ECD for the 8.9 mg/mL sample (one of the 4 concentrations tested). Over all the samples recorded, an overall radius of gyration (Rg) of 3.07±0.08 nm and a largest particle dimension (Dmax) of 10.48 ± 0.7 nm were obtained for the hDCIR-ECD dimer.

(D) Model of the topological presentation of hDCIR dimer within the plasma membrane.

(E) Structural superposition of hDCIR-ECD structure (in pink) and hDCIR-CTLD (*i.e.*, C-type lectin-like domain in blue; PDB 5b1x). Protein, carbohydrate, and calcium ions are shown in ribbon (pink/blue), stick (green/red), and sphere (light blue) models, respectively.

(F) Two-dimensional interaction maps of the Galα1-3Galβ1-4GlcNAcβ1-2Manα antennas of biantennary complex-type N-glycan bound to hDCIR-ECD conformers A and B. The hydrogen bonds and coordination involved in the interaction between the ligand, the calcium ion, and atoms of the protein residues are represented by dotted green lines. Van der Waals contact between the ligand and the protein are represented by notched semicircles. The 2D interaction maps were designed based on Ligplot+ v.2.2 (https://www.ebi.ac.uk/thornton-srv/software/LigPlus/)

(G) Sequence alignment of human DCIR and mouse DCIR homologues (mDCIR1-4) as generated using ESPript 3.0 (https://espript.ibcp.fr/ESPript/ESPript/index.php). The secondary structure shown corresponds to that of human DCIR.

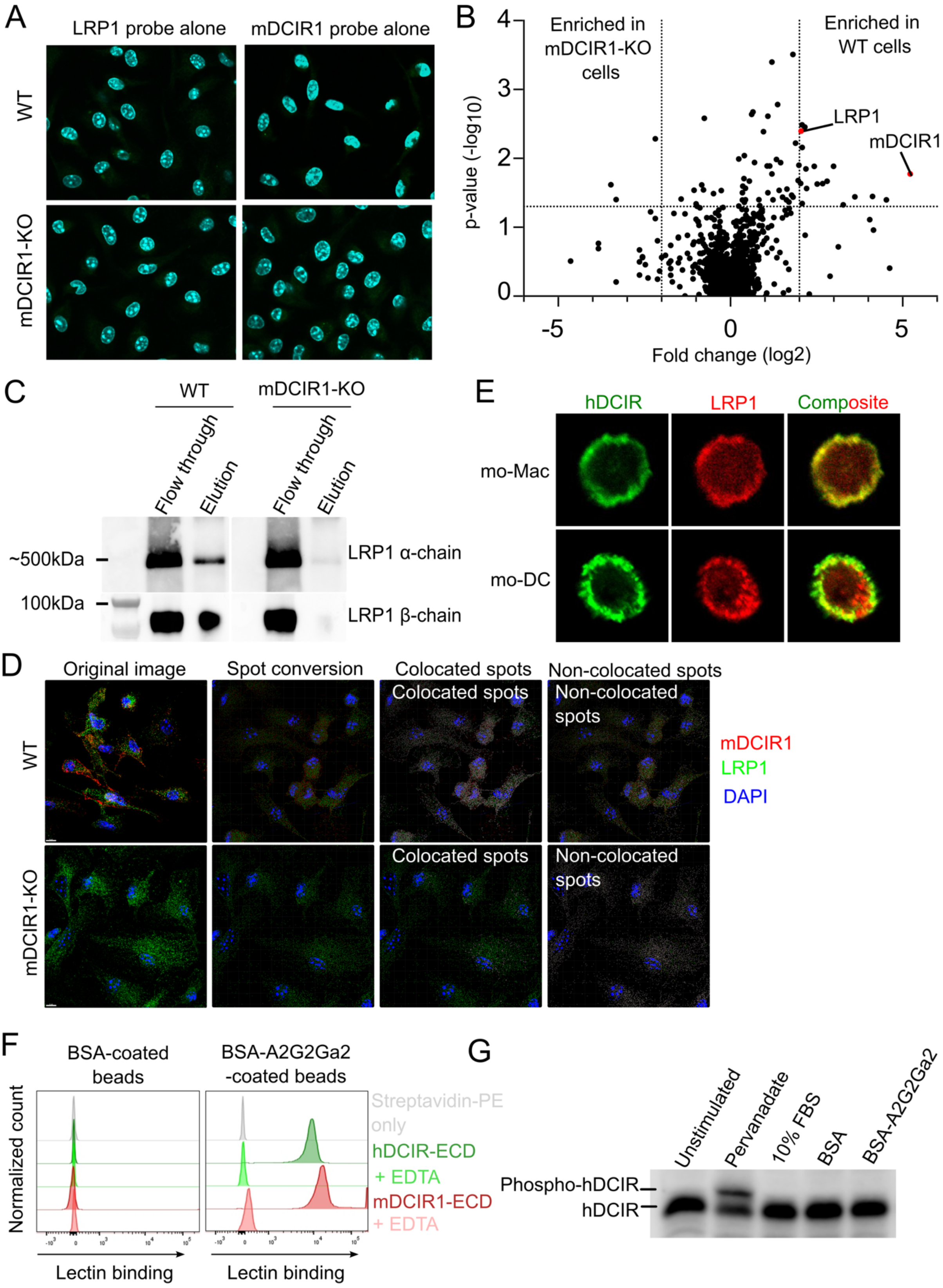
A
LRP1 probe alone
mDCIR1 probe alone
WT
mDCIR1-KO
B
Enriched in mDCIR1-KO cells
Enriched in WT cells
LRP1
mDCIR1
p-value (-log10)
4
3
2
1
0
-5
0
5
Fold change (log2)
C
WT
mDCIR1-KO
Flow through
Elution
Flow through
Elution
~500kDa
100kDa
LRP1 α-chain
LRP1 β-chain
E
hDCIR
LRP1
Composite
mo-Mac
mo-DC
D
Original image
Spot conversion
Colocated spots
Non-colocated spots
Colocated spots
Non-colocated spots
WT
mDCIR1-KO
mDCIR1
LRP1
DAPI
F
BSA-coated beads
BSA-A2G2Ga2 -coated beads
Streptavidin-PE only
hDCIR-ECD
+ EDTA
mDCIR1-ECD
+ EDTA
Normalized count
Lectin binding
Lectin binding
G
Unstimulated
Pervanadate
10% FBS
BSA
BSA-A2G2Ga2
Phospho-hDCIR
hDCIR

Figure S7: Investigation of the spatial proximity between DCIR and LRP1, and the mechanism of DCIR activation (related to figure 7).

(A) Confocal fluorescence images of WT and mDCIR1-KO BMDMs show no detectable proximity ligation assay (PLA) signal when using oligonucleotide-conjugated anti-LRP1 or anti-mDCIR1 antibodies individually. DAPI staining (cyan) confirms the presence of both WT and mDCIR1-KO BMDMs.

(B) Volcano plot from proteomics analysis of affinity-purified, biotinylated proteins differentially enriched (X-axis: $\log_2$ fold change) in WT versus mDCIR1-KO BMDMs following proximity labeling with biotin tyramide reagent and a horseradish peroxidase (HRP)-conjugated anti-mDCIR1 antibody. Statistical significance is shown on the Y-axis ($-\log_{10}$ *p*-value). Statistical analysis was performed using a paired Student's *t*-test. Dashed line marks the threshold limit ($\log_2$ fold change ≥ +/- 2 and $-\log_{10}$ *p*-value ≥ 1.301).

(C) Western blot analysis confirms the presence of LRP1 α- and β-chains in WT BMDMs, but not in mDCIR1-KO cells, in affinity-purified biotinylated proteins resulting from the proximity labeling with biotin tyramide reagent and anti-HRP-conjugated mDCIR1 antibody.

(D) Conversion of fluorescence of LRP1 and mDCIR1 signals into spots from super-resolution structured illumination microscopy images of WT and mDCIR1-KO BMDMs.

(E) Confocal fluorescence imaging of peripheral blood monocyte-derived macrophages (mo-Macs) and dendritic cells (mo-DCs) showing a clear colocalization pattern of LRP1 and hDCIR.

(F) Flow cytometry histograms of the binding of biotinylated hDCIR-ECD and mDCIR1-ECD coupled to Streptavidin-Phycoerythrin (Streptavidin-PE), in the absence or presence of divalent cation chelating agent EDTA, to microspheres coated with bovine serum albumin (BSA) or α-Gal-containing biantennary complex-type N-glycans linked to BSA (BSA-A2G2Ga2).

(G) Western blot analysis of phosphorylated hDCIR in mo-DCs either left unstimulated, treated with pervanadate for 15 minutes, or cultured for 30 minutes on wells coated with 10% serum, bovine serum albumin (BSA), or α-Gal-containing biantennary complex-type N-glycans conjugated to BSA (BSA-A2G2Ga2)